

Calcium triplet metallicity calibration for stars in the Galactic bulge^{★,★★}

S. Vásquez^{1,2,9}, M. Zoccali^{1,2}, V. Hill³, O. A. Gonzalez⁴, I. Saviane⁴, M. Rejkuba^{5,8}, and G. Battaglia^{6,7}

¹ Instituto de Astrofísica, Pontificia Universidad Católica de Chile, Av. Vicuña Mackenna 4860, 782-0436 Macul, Santiago, Chile
e-mail: svasquez@astro.puc.cl

² Millennium Institute of Astrophysics, Av. Vicuña Mackenna 4860, 782-0436 Macul, Santiago, Chile

³ Laboratoire Lagrange (UMR7293), Université de Nice Sophia Antipolis, CNRS, Observatoire de la Côte d'Azur, CS34229,
06304 Nice Cedex 4, France

⁴ European Southern Observatory, Av. Alonso de Cordova 3107, Casilla 19, 19001 Santiago, Chile

⁵ European Southern Observatory, Karl-Schwarzschild-Strasse 2, 85748 Garching, Germany

⁶ Excellence Cluster Universe, Boltzmannstr. 2, 85748 Garching, Germany

⁷ Instituto de Astrofísica de Canarias, calle via Láctea s/n, 38205 San Cristobal de La Laguna, Tenerife, Spain

⁸ Universidad de La Laguna, Dpto. Astrofísica, 38206 La Laguna, Tenerife, Spain

⁹ Museo Interactivo Mirador, Dirección de Educación, Av. Punta Arenas, 6711 La Granja, Santiago, Chile

Received 14 May 2015 / Accepted 29 June 2015

ABSTRACT

Aims. We present a new calibration of the calcium II triplet equivalent widths versus [Fe/H], constructed upon K giant stars in the Galactic bulge. This calibration will be used to derive iron abundances for the targets of the GIBS survey, and is in general especially well suited for solar and supersolar metallicity giants, which are typical of external massive galaxies.

Methods. About 150 bulge K giants were observed with the GIRAFFE spectrograph at the VLT with a resolution of $R \sim 20\,000$ and at $R \sim 6000$. In the first case, the spectra allowed us to directly determine the Fe abundances from several unblended Fe lines, deriving what we call here high-resolution [Fe/H] measurements. The low-resolution spectra allowed us to measure equivalent widths of the two strongest lines of the near-infrared calcium II triplet at 8542 and 8662 Å.

Results. By comparing the two measurements, we derived a relation between calcium equivalent widths and [Fe/H] that is linear over the metallicity range probed here, $-1 < [\text{Fe}/\text{H}] < +0.7$. By adding a small second-order correction based on literature globular cluster data, we derived the unique calibration equation $[\text{Fe}/\text{H}]_{\text{CaT}} = -3.150 + 0.432W' + 0.006W'^2$, with an rms dispersion of 0.197 dex, valid across the whole metallicity range $-2.3 < [\text{Fe}/\text{H}] < +0.7$.

Key words. stars: abundances – Galaxy: bulge – techniques: spectroscopic

1. Introduction

The calcium II triplet (CaT) at ~ 8500 Å is one of the most widely used metallicity indices as well as an excellent feature for measuring radial velocity at low spectral resolution. The three lines at 8498, 8542, and 8662 Å are so strong that they can be easily measured at low resolution and at relatively low signal-to-noise ratio (S/N). In addition, their location in the near-infrared part of the spectrum is ideal to observe the brightest stars of any not too young stellar population, namely cool giants. CaT spectra of cool giants can be obtained with reasonable exposure time both for external galaxies in the local group, which are too far away to be observed at high spectral resolution, and for Milky Way stars in high-extinction regions, such as the Galactic bulge.

The popularity of the CaT spectral feature obviously resides in how accurately it can be used to measure metallicities. Armandroff & Zinn (1988) first demonstrated that the equivalent widths (EWs) of CaT lines in the integrated spectra of globular clusters (GCs) strongly correlate with the cluster metallicity [Fe/H]. A few years later, Olszewski et al. (1991),

Armandroff & Da Costa (1991) analysed the behaviour of CaT lines in individual cluster stars. They noted that the EWs of CaT lines show a dependence not only on metallicity, but also on absolute magnitude. They therefore introduced the use of “reduced equivalent widths” (W'), which corresponds to the sum of some combination of the individual EWs, weighted by the difference between the stellar V magnitude and the magnitude of the horizontal branch in the same cluster ($V - V_{\text{HB}}$).

Several empirical relations between the reduced EWs of CaT lines and the [Fe/H] abundance are present in the literature. Most of them used star clusters, for which the [Fe/H] abundance could be derived in several ways, and not necessarily for the same stars for which CaT was measured. Among these, a very comprehensive work was published by Rutledge et al. (1997), who derived CaT metallicities for 52 Galactic GCs in a homogeneous scale, covering the range $-2 < [\text{Fe}/\text{H}] < -0.7$. By comparing their scale with the classical Zinn & West (1984) metallicity scale, they found a non-linear relation between the two. Conversely, a linear relation was found between the CaT metallicities by Rutledge et al. (1997) and the metallicities derived by Carretta & Gratton (1997). The latter are based on Fe lines measured on high-resolution spectra.

Traditionally, the CaT metallicity calibration has been constructed based on RGB stars in globular (Cole et al. 2004; Warren & Cole 2009; Saviane et al. 2012, e.g.) or open clusters

* Based on observations taken with ESO telescopes at the La Silla Paranal Observatory under programme ID 385.B-0735(B).

** Full Table 2 is only available at the CDS via anonymous ftp to cdsarc.u-strasbg.fr (130.79.128.5) or via <http://cdsarc.u-strasbg.fr/viz-bin/qcat?J/A+A/580/A121>

(Carrera et al. 2007, 2013). Open clusters allowed Carrera et al. to extend the metallicity range up to $[\text{Fe}/\text{H}] \sim +0.5$, at the same time probing a younger age regime ($13 \text{ Gyr} < \text{age} < 0.25 \text{ Gyr}$). The CaT EWs seem to be only weakly dependent on the age of the star, although only a few star clusters constrain the relation at high metallicity, and old star clusters at supersolar metallicities are not available to set a robust constraint on the age dependence.

Battaglia et al. (2008) compared a CaT calibration based on GCs with one based on red giants in dwarf spheroidal galaxies. The latter are complex stellar populations with a range of ages and, most importantly, a range of $[\text{Ca}/\text{Fe}]$ abundance ratio. They concluded that the two relations are fairly consistent within the errors, although small differences exist. In particular, a CaT-to- $[\text{Fe}/\text{H}]$ calibration based on GCs would overestimate the $[\text{Fe}/\text{H}]$ of low metallicity stars ($[\text{Fe}/\text{H}] < -2.2$) by ~ 0.1 dex, while underestimating the $[\text{Fe}/\text{H}]$ of (relatively) high-metallicity stars ($[\text{Fe}/\text{H}] > -1.2$) by ~ 0.1 – 0.2 dex. It is important to emphasise that their analysis is limited to the metallicity range $-2.5 < [\text{Fe}/\text{H}] < -0.5$.

More recently, Starkenburg et al. (2010) presented a synthetic spectral analysis of the CaT method to derive iron abundance, with particular emphasis on the low-metallicity regime. They derived a new calibration, valid in the range $-4 < [\text{Fe}/\text{H}] < -0.5$, which deviates from the commonly used linear relation for $[\text{Fe}/\text{H}] < -2$.

To summarise, CaT to $[\text{Fe}/\text{H}]$ calibrations at solar and super-solar metallicities are very sparse and based only on young open clusters. Deviations from linearity, in the relation between CaT EWs and $[\text{Fe}/\text{H}]$ in the high-metallicity regime are to be expected, given that the calcium lines are highly saturated already well below solar metallicity. Departures from local thermodynamical equilibrium are also known to affect the core of the lines (Mashonkina et al. 2007) because of saturation. In this paper we probe the high-metallicity regime of this relation based on old red giants in the Galactic bulge.

This study is the result of a pilot project we carried out to investigate the possibility of deriving the metallicity distribution function (MDF) of the Galactic bulge based on an iron abundance scale by measuring CaT lines in low- to intermediate-resolution GIRAFFE spectra. To this end, we acquired both high ($R \sim 20\,000$) and low ($R \sim 6\,000$) resolution GIRAFFE spectra for a large sample of K giants in two fields in the Galactic bulge. When preliminary results were very encouraging, we were granted an ESO Large Programme (187.B-0909; PI: Zoccali) to observe 200–400 red clump (RC) giants in each of the 25 fields in the Galactic bulge with GIRAFFE at low resolution. These were then combined with other archive data obtained with the same instrument and setup, also targeting bulge RC stars. The resulting dataset, including spectra for 6392 stars in 31 fields, is called the Giraffe Inner Bulge Survey (GIBS), described in (Zoccali et al. 2014, hereafter Paper I). Paper I also lists the radial velocity of individual stars in the sample and presents radial velocity and velocity dispersion maps of the inner bulge.

We focus here on the CaT to $[\text{Fe}/\text{H}]$ calibration that will be used in a forthcoming paper to derive the MDF in 25 fields in the Galactic bulge.

2. Observation and data reduction

The target stars we used to construct the CaT calibration are all located in Baade’s Window, and they consist of two samples: 80 stars in the bulge RC and 68 stars on the RGB, which are ~ 0.7 mag brighter than the RC. The medium-resolution spectra

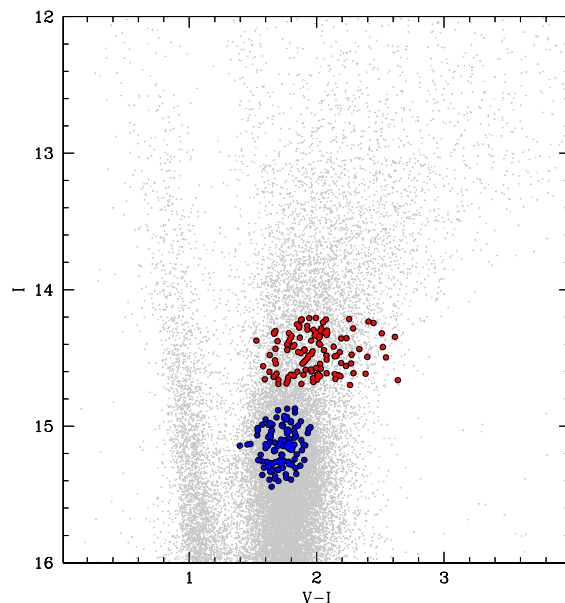


Fig. 1. Target selection is shown over the V - and I -band colour magnitude diagram using coloured dots. Red and blue dots correspond to the RC and RGB stars from Baade’s Window ($b = -4$).

analysed here were taken with the FLAMES-GIRAFFE multifibre spectrograph at the VLT, in Medusa mode, within the ESO program ID 385.B-0735(B). The spectrograph allows us to obtain spectra for ~ 130 objects, including sky positions, over a 25 arcmin diameter field of view. We selected the LR08 setup, which covers the wavelength range between 8206 and 9400 Å, with a spectral resolution of $R \approx 6500$. The exposure time needed to reach a mean S/N of $\sim 50/\text{pix}$ were 900 and 1800 s for RGB and RC stars, respectively.

High-resolution spectra for the targets in Baade’s Window were obtained from Zoccali et al. (2008) and Hill et al. (2011), who used the same instrument in the setups HR13 and HR14 with a resolution of $R \approx 22\,500$ and $R \approx 28\,800$, respectively. Figure 1 shows the corresponding colour magnitude diagrams (CMDs) for the target selection.

The data were reduced using the instrument pipeline provided by ESO (version 2.8), which performs bias subtraction, flat-field corrections, wavelength calibration, and 1D extraction based on the daytime calibration images. Since the pipeline does not include the sky subtraction routine, we performed this task with IRAF as follows. As a first step, a master sky spectrum was created by combining all the sky spectra (~ 20 per setup) using the median and a sigma-clipping algorithm. Figure 2 (upper panel) shows the raw spectrum of a typical star, around the CaT region, together with the master sky spectrum for the same exposure. It is clear that the three CaT lines do not suffer from strong contamination from sky emission lines compared with CaT line strength. The master sky spectrum was then subtracted from each individual science spectrum using the IRAF task `skytwave`. The latter allows shifting and scaling of the master sky spectrum until a good subtraction is achieved. To find the best shift and scale factor, we used the strong emission lines located in the wavelength range between 8261 to 8481 Å and 8739 to 9071 Å.

The spectra were normalised with the IRAF task `continuum`, using the wavelength range between 8250–8461 Å, 8568–8650 Å, and 8700–9273 Å to avoid the CaT lines. Finally, radial velocities were measured by means of cross-correlation (`fxcor` task) against a template synthetic spectrum

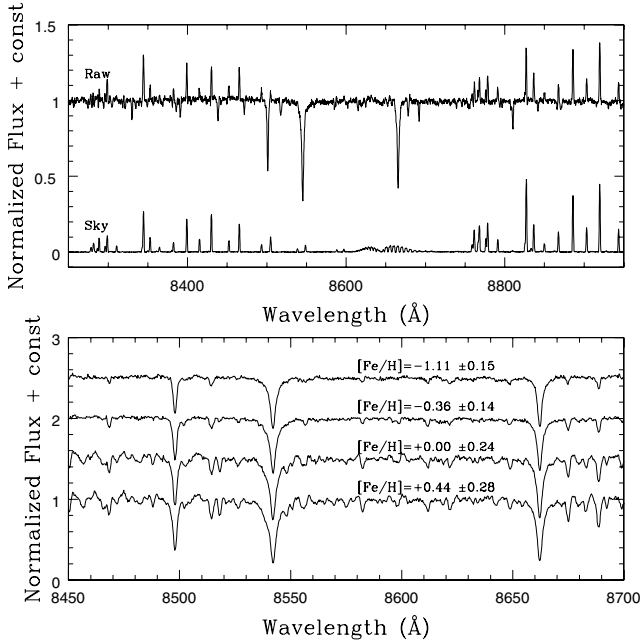


Fig. 2. *Upper panel:* normalised raw spectrum for a typical Milky Way bulge star together with the corresponding sky spectrum. The *lower panel* shows processed spectra for four bulge stars spanning the typical metallicity range of the Galactic bulge. The increasing strength of the CaT lines with metallicity is evident, as is the increasing number of small atomic lines contaminating the continuum.

for a typical metal poor K giant star ($T_{\text{eff}} = 4750$, $\log g = 2.5$ and $[\text{Fe}/\text{H}] = -1.3$). This low metallicity was chosen to ensure that the CaT lines in the template were relatively deep but free of contaminations by other lines on their wings.

Example of the final spectra, sky subtracted, radial velocity corrected, and continuum normalised, are shown in the lower panel of Fig. 2 for stars of different metallicities. An arbitrary shift was applied along the y -axis to avoid overlaps.

3. Calcium triplet calibration

The spectral region around the CaT feature (8350–9000 Å) includes several lines that might dominate the spectrum, depending on the spectral type of the star under analysis. Cenarro et al. (2001) showed that stars with spectral type between F5 ($T_{\text{eff}} \sim 6500$ K) and M2 ($T_{\text{eff}} \sim 3700$ K) are the best targets to measure the CaT lines because they are only marginally contaminated by FeI, MgI, and TiI lines. CaT lines in hotter stars are blended with Paschen lines, while in cooler stars the continuum is plagued by TiO molecular bands. Being of K spectral type, our targets are well inside the recommended temperature range.

Additional constraints have been proposed in terms of the brightness range where a single gravity correction can be used (see Sect. 3.2 for details). Carrera et al. (2007) defined a minimum absolute magnitude $M_V \leq 1.25$ or $M_I \leq 0.0$, while Da Costa et al. (2009) recommended a lower brightness limit of ~ 0.2 mag below the RC (or the horizontal branch). Both our RGB and RC targets are inside these constraints, with the RC stars being within the intrinsic dispersion – mainly due to metallicity and distance spread – of the RC in Baade’s Window.

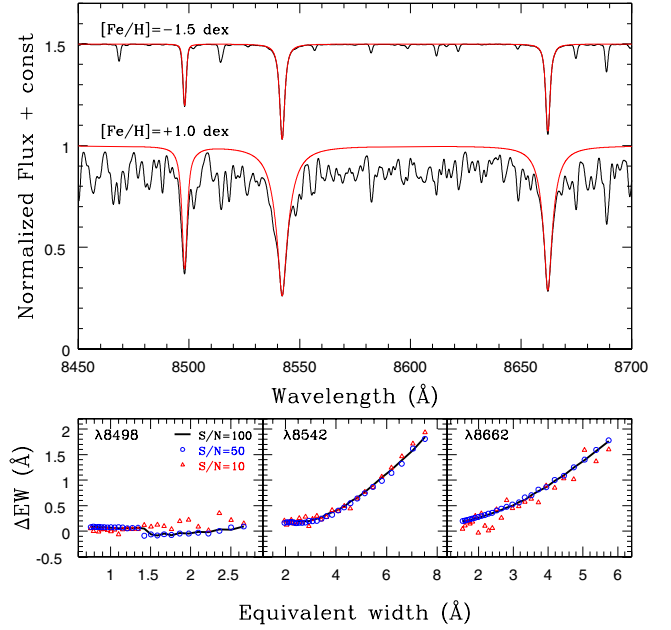


Fig. 3. *Upper panel:* comparison between the more metal poor and metal rich synthetic spectra from our library, in the region around the CaT lines. In both cases, the black line shows the spectra including the lines of all elements, while the red lines shows only the three CaT lines. The *lower panels* show the difference between the *real* EW, as measured in the red spectra, and the *measured* EW, as measured in the black spectra, for each of the three CaT lines as a function of EW and for three values of S/N.

3.1. Equivalent width measurements

While both our RC and RGB target stars are inside the recommended temperature and gravity range for CaT measurements, the metallicity distribution of the Galactic bulge reaches (extends) to significantly higher metallicity than typical star clusters for which this calibration has been defined and used so far. The impact of the metal content over the CaT EWs measurements is mostly driven by the continuum depletion due to the increasing contamination of the CaT lines by other atomic lines. To explore the impact of the metal content on the CaT EWs measurement, we analysed a grid of synthetic spectra generated using *turbospectrum*. This is a line synthesis code described in Alvarez & Plez (1998) and improved along the years by B. Plez. In this case, it was used together with the grid of OSMARCS spherical model atmospheres¹ (Gustafsson et al. 2008). The synthetic spectra have the same resolution as the GIRAFFE spectra and a set of stellar parameters representative of a K giant star ($T_{\text{eff}} = 4750$ and $\log g = 2.5$). Only the metallicity was allowed to vary across the range from $[\text{Fe}/\text{H}] = -1.5$ to the extreme case of $[\text{Fe}/\text{H}] = +1.0$ dex², keeping $[\text{Ca}/\text{H}] = [\text{Fe}/\text{H}]$ in the whole grid.

Synthetic spectra for stars at the two extreme ends of the metallicity grid are plotted in the upper panel of Fig. 3. The black line is the synthetic spectrum containing a list of all the elements in the wavelength range between 8450 and 8700 Å. The red line, in contrast, shows only the three CaT lines. This exercise clearly shows the depletion of the continuum (pseudo-continuum) at high metallicity that is due to the presence of many unresolved

¹ Models available at <http://marcs.astro.uu.se/>

² The metallicity distribution of the Milky Way bulge spans the range between -1.5 up to $+0.7$ dex.

Table 1. Line bandpass used in this work.

Feature (Å)	Line bandpass (Å)
8498.02	8491.02–8505.02
8542.09	8530.09–8554.09
8662.14	8653.14–8671.14

lines. Because we studied normalised spectra (without flux calibration), we need to include the effect of continuum depletion in the empirical calibration itself.

The CaT EWs can be measured by fitting an empirical function to each line profile and calculate the corresponding EW from direct integration of the function. Different functions have been explored over the years. [Armandroff & Da Costa \(1991\)](#) used a Gaussian profile when fitting stars in globular clusters. [Rutledge et al. \(1997\)](#) used a Moffat function instead. Both functions only give good results for stars of relatively low metallicity. [Cole et al. \(2004\)](#) showed that in the metal-rich regime, the strong wings of the CaT lines can be reproduced by the sum of a Gaussian component, fitting the line core, and a Lorentzian function, fitting the wings. [Erdelyi-Mendes & Barbuy \(1991\)](#) and [Battaglia et al. \(2008\)](#) showed that the EWs of CaT lines is driven mostly by the wings because of the strong pressure broadening. In other words, the strength of the line is mostly driven by the electronic pressure (i.e. metallicity), not by the usual combination of temperature and elemental abundance, shaping weak lines.

To test the accuracy of the Gaussian+Lorentzian fit across a range of metallicity and S/Ns, we performed some measurements on the grid of synthetic spectra described above. As a first step, EWs were measured in the synthetic spectra containing only calcium lines by means of numerical integration. These were assumed to be the real EWs. As a second step, the grid of synthetic spectra was convolved to the resolution and resampled in wavelength to match real data and degraded to different S/N, from 10 to 100 in steps of 10. A Poisson noise model was used for the last operation. The resulting spectrum was then renormalised to a pseudo-continuum of 1, and the combination of a Gaussian and a Lorentzian function was fitted to the CaT lines. The wavelength ranges used by [Armandroff & Zinn \(1988\)](#) for the fit were slightly modified, as listed in Table 1, to improve the fit of the wings. The lower panel of Fig. 3 shows the difference between the measured and the real EWs for each of the CaT lines as a function of EW (metallicity) and S/N. It is clear that the EWs of the two strong lines would be underestimated in the data, and more so at high metallicities. This systematic reaches up to ~ 1 Å around $[\text{Fe}/\text{H}] = +0.5$. However, the trend is very smooth and is not affected by S/N, down to a $S/N \sim 10$, much lower than our poorest spectrum. As a consequence, a correction for this systematic is implicitly included in the $[\text{Fe}/\text{H}]$ -vs.-CaT empirical calibration equation derived in Sect. 3.4. For the weakest line, the systematic difference between real and measured EW is much smaller than for the strong lines. However, a step is found around $EW_1 = 1.5$ Å that is due to the appearance of some blends in the wings of this line. Additionally, the weakest line is the most affected by imperfect sky subtraction because of the presence of two sky lines close to its wings. For this reason, we discarded this line in the following analysis.

Examples of line fitting are shown in Fig. 4 for three observed spectra covering the metallicity range of the Milky Way bulge. For each star, the large black dots show the observed spectrum, the red line is the final fit, while the thin dotted and dashed

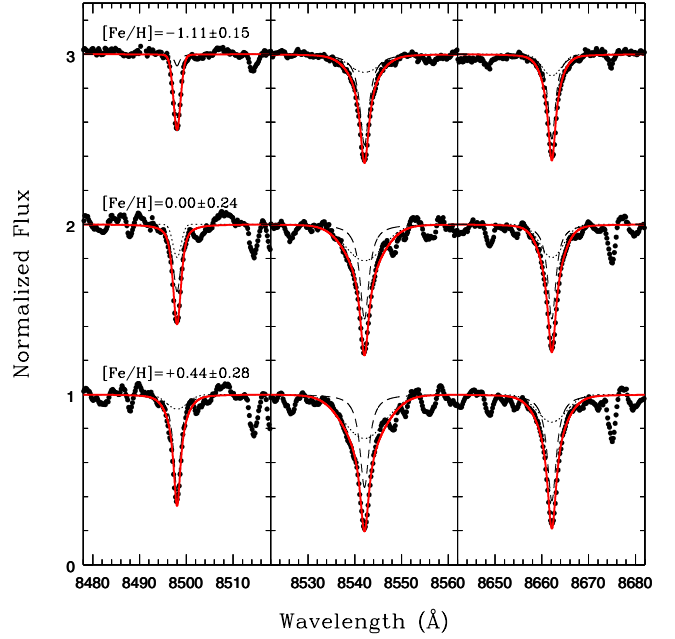


Fig. 4. Fitting examples for three bulge stars covering the metallicity range of the Milky Way bulge. The red line corresponds to the best-fitting function found for each line, while we plot the individual contribution from Gaussian and Lorentzian functions as dashed lines.

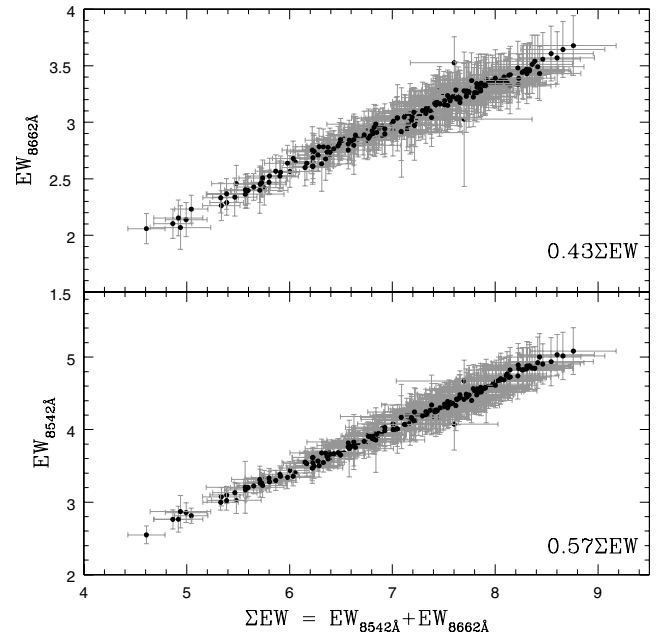


Fig. 5. Strength of the two strongest CaT lines versus the sum of the two lines, ΣEW . The corresponding fractional contribution with respect to ΣEW is shown in each panel.

lines show the individual contribution of the Gaussian and the Lorentzian profiles, respectively. Additionally, the line-ratio between the two strongest CaT lines is remarkably constant across the metallicity range spanned by the bulge data. Figure 5 shows the contribution of the two strongest individual CaT lines to the sum of the two. The data can be fitted by a single line, with the slope indicated in the label. This line ratio can be used, for instance, to predict the EW of one of the lines, when the other is not available for a direct measurement. It can also be used to test the consistency of the measurements, in order to reject lines

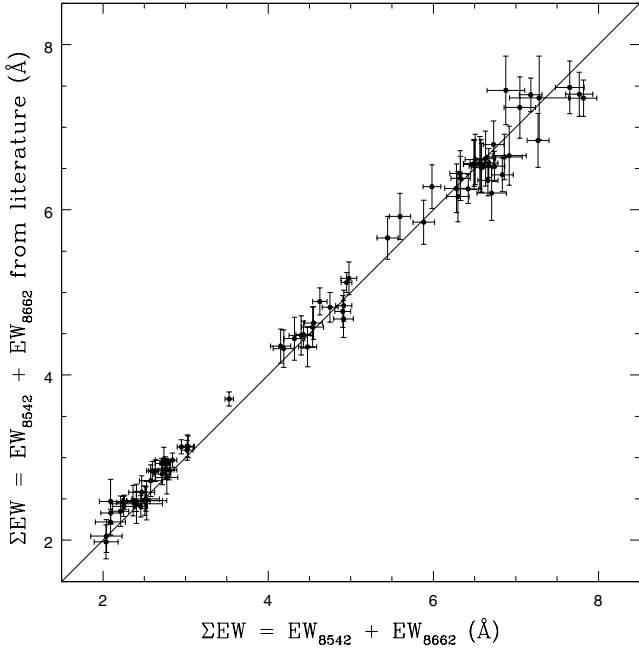


Fig. 6. Comparison between our measurements and the literature values of the sum of the two strongest lines for different stellar clusters taken from Warren & Cole (2009) and Saviane et al. (2012).

with anomalous line ratio. This is particularly useful when dealing with large surveys.

As we explain in the following sections, we used cluster stars to constrain the final metallicity CaT calibration. Before doing this, we need to verify that our EW measurements are on the same scale as those used in previous works. To this end, we obtained the spectra of the two most metal-rich clusters (NGC 6791 and NGC 6819) in the sample by Warren & Cole (2009) and re-measured the EWs. The spectra kindly provided to us, by private communication, were already wave-calibrated and sky-subtracted, therefore we only applied the same continuum normalisation procedure and EW measurement used for our data. Additionally, to probe a wider range of metallicity, we also measured a sample of globular cluster stars, drawn from Saviane et al. (2012), spanning the metallicity range $-2.3 < [\text{Fe}/\text{H}] < +0.07$. The selected stars belong to the globular clusters M 15, NGC 6397, M4, NGC 6553, and NGC 6528. Figure 6 shows the excellent agreement between our measurements and those in the literature for the sum of the EWs of the two strongest CaT lines, hereafter $\Sigma EW (= EW_{8542} + EW_{8662})$.

3.2. Reduced equivalent width

The strength of an atomic line, in general, is driven by the elemental abundance, the effective temperature, and the surface gravity of the star. Both Armandroff & Da Costa (1991), Olszewski et al. (1991) showed that the combined effect of effective temperature and surface gravity on the EWs of CaT lines can be parametrised as a function of luminosity alone. The CaT EWs corrected by this effect (i.e. the reduced EWs) only depend upon metallicity. Specifically, the authors found that in each given cluster, red giant stars follow a straight line in the luminosity– ΣEW plane. The slope of the line is identical for different clusters, while its zero point depends on the cluster metallicity. As a proxy for luminosity, some authors used the absolute magnitude of the star (Carrera et al. 2007, 2013), or, most

commonly, the difference between the star apparent magnitude and the magnitude of the cluster horizontal branch, or red clump (Armandroff & Da Costa 1991; Rutledge et al. 1997; Cole et al. 2004; Battaglia et al. 2008; Warren & Cole 2009; Saviane et al. 2012; Mauro et al. 2014). We adopted the second option to minimise the uncertainty in the distance and reddening, both variable across the Galactic bulge.

The K_s magnitude, from the VVV survey (Minniti et al. 2010), was used for our bulge stars. To determine the slope in the luminosity– ΣEW plane, we used the star cluster data from Warren & Cole (2009). For each cluster star we plotted ΣEW as a function of $(K - K_{\text{RC}})$ and fitted a linear relation, deriving a representative slope by making the average of the single measurements. The left panel of Fig. 7 shows the straight lines defined by different clusters, each in a different colour. They are consistent with a constant slope of $\beta_{K_s} = 0.384 \pm 0.019 \text{ \AA mag}^{-1}$, in excellent agreement with those derived by Mauro et al. (2014) using the clusters from Saviane et al. (2012) combined with VVV photometry. This slope allows us to define the reduced EW parameter

$$W' = \Sigma EW + \beta_{K_s} (K - K_{\text{RC}}),$$

which is only dependent upon the metallicity of the star.

To determine the corresponding $(K - K_{\text{RC}})$ for our bulge stars, we measured the mean RC magnitude from the complete VVV de-reddened K_s photometric catalogue corresponding to the observed field by using the reddening map presented in Gonzalez et al. (2011b). The right panel of Fig. 7 shows the location of our RC and RGB targets, all in Baade’s Window, in the same plane. The colour coding traces metallicity (as measured from the HR spectra), and it is the same as was used for the star clusters. Contrary to what happens in star clusters, bulge stars in each metallicity bin do not seem to define parallel straight lines. We interpret this as the result of the probable disk contamination, the error bar on the metallicity of each star, and the intrinsic width of the metallicity bin. Moreover, while for star clusters the x -axis is a clean proxy for luminosity, bulge stars have a significant distance spread, and the red clump only reflects their mean distance.

3.3. Reference metallicities: galactic bulge and globular clusters

To derive an equation converting between W' and the $[\text{Fe}/\text{H}]$ abundances, a set of independent determinations of $[\text{Fe}/\text{H}]$ from high-resolution spectra are needed. In what follows we describe how these were obtained for bulge field giants and for a subset of the globular clusters presented in Warren & Cole (2009). The latter were added to our sample after we determined that they were fully compatible, so that we could extend the metallicity range on the metal-poor side.

3.3.1. Homogeneous high-resolution metallicities determination for Galactic bulge stars

$[\text{Fe}/\text{H}]$ abundances for both RC and RGB stars in Baade’s Window were discussed in Zoccali et al. (2008) and Hill et al. (2011). They were based on GIRAFFE spectra through set-ups HR13 and HR14 with a resolution of $R \sim 22\,500$ and $\sim 28\,800$, respectively. After the pre-reduction and coaddition of the spectra explained in Sect. 2, iron abundances were measured by means of individual unblended iron lines. Conceptually, we used the same method as explained in our previous works,

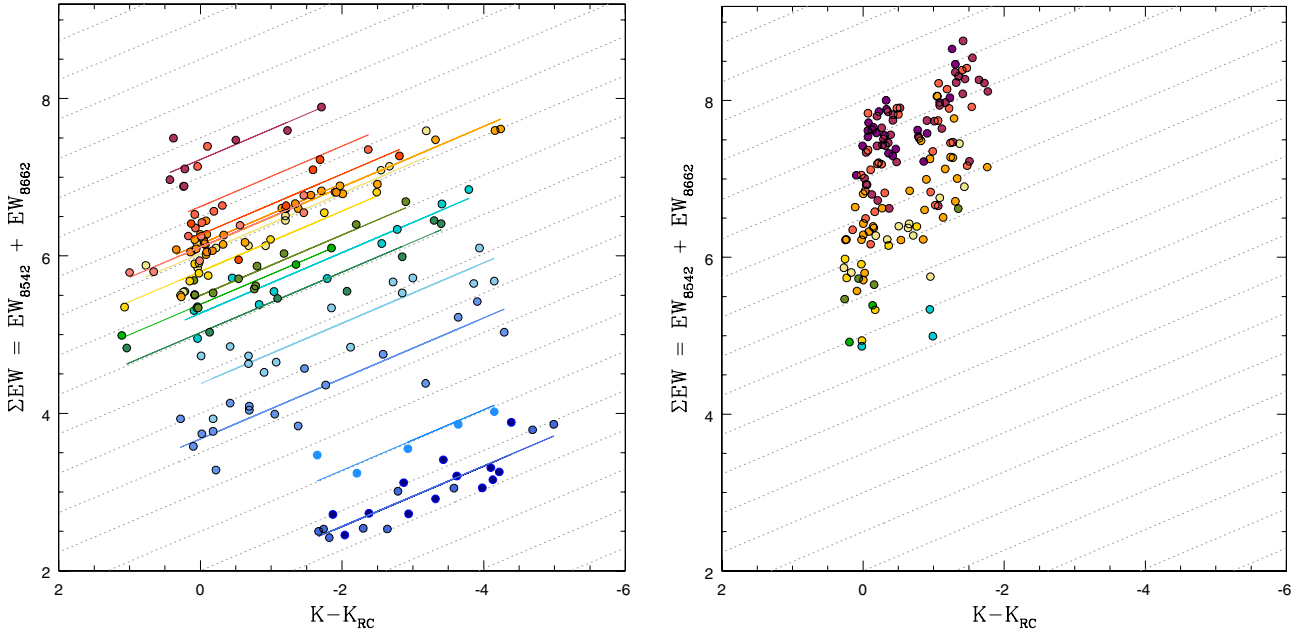


Fig. 7. CaT equivalent widths of the star cluster RGBs (*left panel*) and Galactic bulge stars (*right panel*) are compared with their corresponding magnitude above the mean red clump magnitude. The colour code is used to mark clusters of different metallicity, together with their best-fitting lines, assuming the best common slope of $0.384 \text{ \AA mag}^{-1}$. The thin dotted lines in each panel show this slope to guide the eye.

cited above. Namely, first-guess effective temperature and gravity were derived from photometry and used to construct an approximate model atmosphere. The latter was used to independently derive $[\text{Fe}/\text{H}]$ abundances from several FeI and FeII lines. The stellar surface parameters (T_{eff} , $\log g$ and the microturbulent velocity χ) were then refined by imposing consistency among the abundances derived from different lines. As discussed in Hill et al. (2011), the actual implementation of this method may yield slightly different final abundances – especially for metal-rich, cold giants – depending on which of the stellar parameters is fixed first. In other words, there can be degeneracies in the parameter space that are due to correlations among the stellar parameters.

To minimise this effect, we here applied an automated procedure based on the use of GALA (Mucciarelli et al. 2013). This code is designed to impose the excitation and ionization equilibria on FeI lines, thus deriving T_{eff} and $\log g$, respectively, and to converge on a value for the microturbulent velocity that yields the same $[\text{Fe}/\text{H}]$ abundance for lines of different EWs. The ATLAS9 (Castelli & Kurucz 2004) model atmospheres were used instead of the MARCS ones (Gustafsson et al. 2008) because GALA is optimised for the former. The results are fully compatible with those of Zoccali et al. (2008) and Gonzalez et al. (2011b). A small offset within the errorbars is present between the resulting metallicities and those presented by Hill et al. (2011). The use of GALA, however, does reduce at least the statistical errors, as demonstrated by the exceptionally small spread of abundances in the $[\text{Mg}/\text{Fe}]$ versus $[\text{Fe}/\text{H}]$ plot, presented in Zoccali et al. (2015) and Gonzalez et al. (2015).

3.3.2. Globular clusters

To constrain the CaT versus $[\text{Fe}/\text{H}]$ calibration in the metal-poor regime, where bulge stars are sparse, we considered adding some globular clusters to our sample. A natural choice was a subset of the cluster sample of Warren & Cole (2009). This is for two main reasons: i) we had access to their spectra, and indeed we

have shown in Fig. 6 that the EWs measured with our method are fully consistent with theirs; ii) K_s photometry is available for all these stars. In their work, Warren & Cole (2009) derived a calibration equation between the CaT reduced EWs, as derived using the three lines, and $[\text{Fe}/\text{H}]$ measured in the scale of Carretta & Gratton (1997). The latter scale, however, has been revised in Carretta et al. (2009; hereafter C09), to what has now become a new standard (e.g. Harris 1996, 2010 edition). We therefore updated the $[\text{Fe}/\text{H}]$ abundances to the C09 scale using the compilation in Carrera et al. (2013). For globular clusters without new $[\text{Fe}/\text{H}]$ measurements, we instead used the relation provided in C09 to transform the metallicity from the old to the new scale. It is worth emphasising here that both globular clusters and bulge stars have the same calcium over iron ratio ($[\text{Ca}/\text{Fe}] \sim +0.4$) at $[\text{Fe}/\text{H}] \sim -1$, where they overlap (Gonzalez et al. 2011a; Carrera et al. 2013).

The calibration by Warren & Cole (2009) includes several open clusters, constraining the metal-rich regime. We excluded these from our analysis because we sample the metal-rich side with a large number of bulge stars, and our goal is to optimise the calibration for bulge-like giants. In Sect. 4 we compare our calibration with open and globular cluster data.

3.4. Metallicity calibration

The calibration equation between W' and $[\text{Fe}/\text{H}]_{\text{HR}}$ was derived by means of an error-weighted least-squares fitting of the data points relative to individual stars, both in the bulge and in globular clusters. This is different from what is usually done for star clusters, where the mean values of $\langle W' \rangle$ and $\langle [\text{Fe}/\text{H}] \rangle$ for each cluster are used. Several fitting functions were tested before concluding that a linear relation was the best choice, because it minimises the artificial saturation of the calibration equation at high metallicity (i.e. a constant metallicity at higher W'). The latter may create an unphysically sharp cut-off in the iron distribution function.

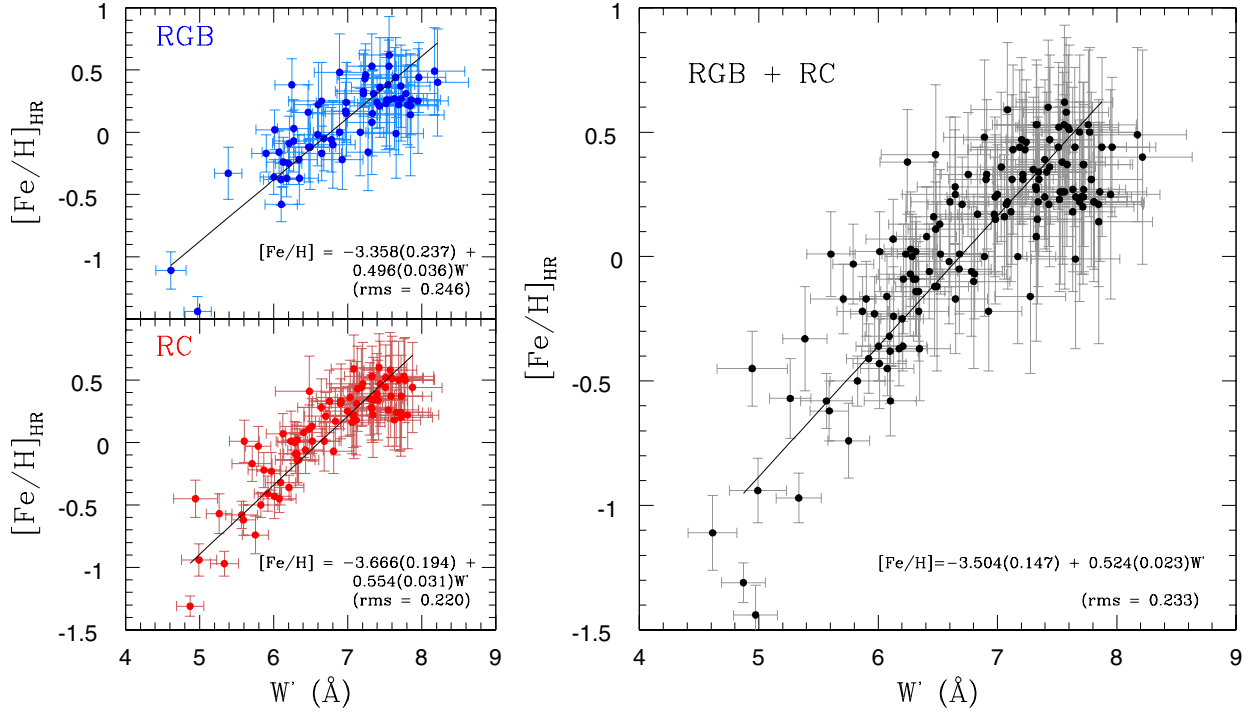


Fig. 8. High-resolution metallicities are compared with reduced equivalent widths of RGB (blue), RC (red) and the combination of the two (black) bulge star samples. The best-fitting CaT calibration for each sample is also shown in each panel.

As a first step, an independent linear fitting was performed between W' and $[\text{Fe}/\text{H}]_{\text{HR}}$ for RGB and RC stars. The results are shown in the left panels of Fig. 8, together with the rms (~ 0.23), which is comparable to the uncertainties of the $[\text{Fe}/\text{H}]_{\text{HR}}$ measurements. The fits are consistent with each other and can therefore be combined in the single linear relation shown in the right panel of the same figure,

$$[\text{Fe}/\text{H}]_{\text{RGB+RC}} = (-3.504 \pm 0.147) + (0.524 \pm 0.023)W', \quad (1)$$

with an rms of 0.233 dex.

As a second step, seven globular clusters were added to the plot, covering the metallicity range $-2.3 < [\text{Fe}/\text{H}] < -0.7$. The fit of a linear relation between the mean W' and mean $[\text{Fe}/\text{H}]$ for the clusters alone yields

$$[\text{Fe}/\text{H}]_{\text{GC}} = (-3.175 \pm 0.094) + (0.462 \pm 0.025)W', \quad (2)$$

which, although slightly different from the equation found for the bulge (Eq. (1)), shows a smooth transition between the two when they overlap. This suggests that a single calibration can be used that is valid across the whole range $-2.3 < [\text{Fe}/\text{H}] < +0.7$. Nevertheless, as globular cluster and Galactic bulge stars do not have the same data sampling (i.e. for globular clusters $\langle W' \rangle$ and $\langle [\text{Fe}/\text{H}]_{\text{HR}} \rangle$ are used instead of the measurements for individual stars), we cannot directly combine the data sets to fit a single function because the resulting fit would be dominated by the metal-poor data, which have smaller errors in $[\text{Fe}/\text{H}]$. Because of this, we decided to create two evenly sampled fiducial data sets taken from Eqs. (1) and (2) in the W' range between $0 < W' < 5.4$ and $5.2 < W' < 10$, respectively. These data sets were then combined into a single one and fitted by a second-order function to take into account the small change of slope between the two linear equations (Eqs. (1) and (2)).

The resulting fit gives

$$[\text{Fe}/\text{H}]_{\text{CaT}} = -3.150 + 0.432W' + 0.006W'^2 \quad (3)$$

with an rms dispersion around the fit of 0.197 dex. No errors are quoted for the coefficients here, because as a result of the procedure adopted to combine globular clusters and bulge stars, this is more a fiducial relation, characterising the locus of the data in the W' versus $[\text{Fe}/\text{H}]$ plane, rather than a formal fit.

When applying the calibration, errors on the derived $[\text{Fe}/\text{H}]$ values were calculated as the quadratic sum of the errors on the EW, propagated through Eq. (3), and the rms of the same equation. Figure 9 summarises our results, showing the final CaT vs. $[\text{Fe}/\text{H}]$ calibration, as a green line, together with the bulge stars (black dots) and the globular clusters (orange dots). For the latter, individual W' measured by Warren & Cole (2009) are plotted for individual stars, all at the same cluster $\langle [\text{Fe}/\text{H}]_{\text{HR}} \rangle$. The upper left corner shows the histogram of the residuals for bulge stars, that is, the differences between $[\text{Fe}/\text{H}]_{\text{HR}}$ and $[\text{Fe}/\text{H}]_{\text{CaT}}$. The distribution is symmetric around zero and the dispersion is consistent with the rms quoted above.

4. Comparison with previous calibrations

Different CaT vs. $[\text{Fe}/\text{H}]$ calibration have been proposed in the past that differ among each other mainly because of the different methods used to measure EWs and the different $[\text{Fe}/\text{H}]$ scales. A recent calibration is presented in Saviane et al. (2012), who used 14 globular clusters to define a cubic equation covering the range $-2.33 < [\text{Fe}/\text{H}] < 0.07$ in the C09 scale. Since the EWs measured by us are fully compatible with those of Saviane et al. (2012) (cf. Fig. 6), the two calibrations can be compared directly as well.

Figure 10 is colour coded in the same way as Fig. 9, with bulge giants as small black dots and globular and open cluster mean values as orange and red dots, respectively (Warren & Cole 2009). Our calibration is shown as a green line. We also show the globular clusters in (Saviane et al. 2012, blue stars) and their calibration equation as a blue dashed line. The two calibrations and

Table 2. Data used in Fig. 8 for the bulge metallicity calibration.

Field	Star ID	RA	Dec	$(K - K_{RC})$	EW_2	σEW_2	EW_3	σEW_3	$[Fe/H]_{HR}$	$\sigma [Fe/H]_{HR}$
RGB	82717	18:04:17.68	-30:00:29.7	-1.643	4.822	0.309	3.441	0.235	0.27	0.41
RGB	423331	18:03:51.67	-29:56:17.6	-0.861	4.127	0.273	3.095	0.205	0.48	0.31
RGB	234704	18:03:25.02	-30:05:01.5	-1.087	3.918	0.179	2.841	0.171	-0.22	0.20
...

Notes. The full table is only available in electronic form at the CDS.

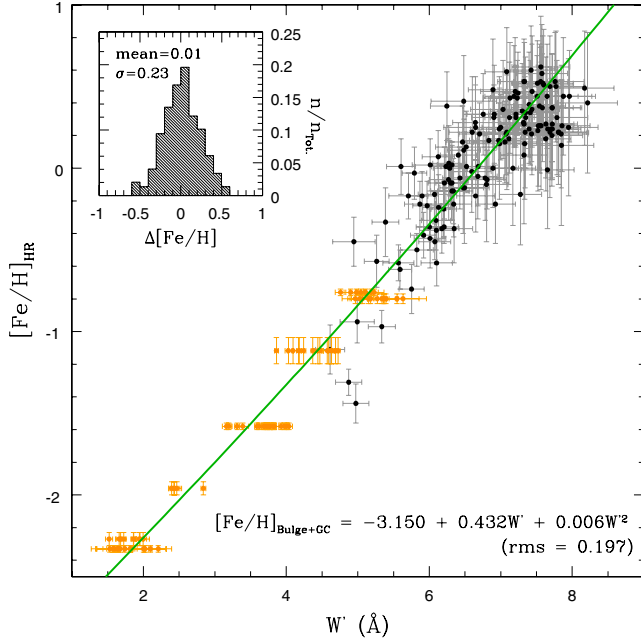


Fig. 9. CaT calibration for the combination between bulge stars (black) with globular clusters from Warren & Cole (2009; orange). The upper left panel shows the corresponding calibration metallicity residuals for bulge stars.

the original one from Warren & Cole (2009) are consistent with each other for $[Fe/H] < -0.8$ dex. The higher order fit in Saviane et al. (2012) is required only by the three most metal-rich globular clusters in their study, namely NGC 5927 ($[Fe/H] = -0.29$), NGC 6553 ($[Fe/H] = -0.16$), and NGC 6528 ($[Fe/H] = +0.07$). Interestingly, the same behaviour is seen in C09, where the updated calibration of Rutledge et al. (1997) changes from a linear to a cubic fit when NGC 6553 is added to the original sample (see Fig. A.2 from Carretta et al. 2009). Moreover, as noted by Saviane et al., NGC 6528 has W' lower than NGC 6553, although it is more metal rich.

Although we are not able to explain the difference between the three most metal-rich globular clusters and bulge stars, we note that the cubic relation of Saviane et al. (2012) is clearly not appropriate for bulge stars, which are the main focus of our interest. We also show in Fig. 10 the open clusters from Warren & Cole (2009). Although the authors originally derived a linear calibration, the use of the updated $[Fe/H]$ from Carrera et al. (2013) for the open clusters is not compatible anymore with a single straight line. The difference between orange dots and red triangles in Fig. 10 looks more like a systematic shift than a change of slope. A similar shift can be observed in the $[Ca/H]$ versus $[Fe/H]$ plot shown in Fig. 11 of Carrera et al. (2013), and it might be ascribed to inhomogeneities in the $[Fe/H]$ sources for open clusters or to a systematic effect that is due to age, compared to globular clusters.

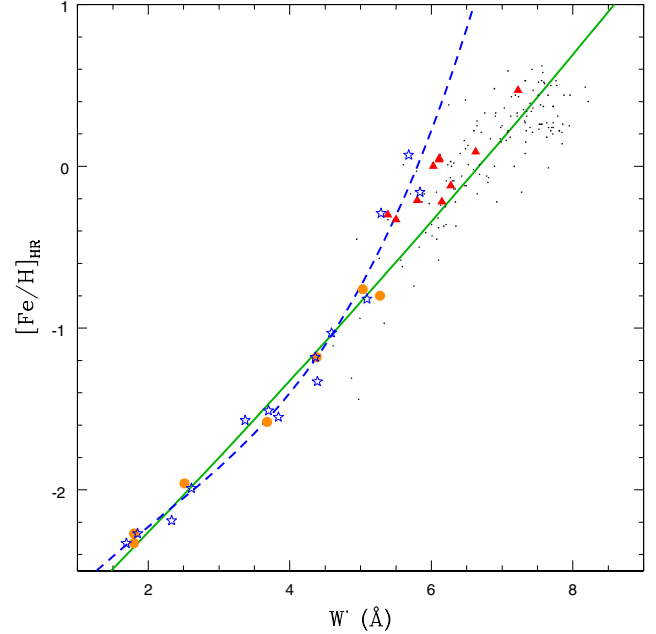


Fig. 10. High-resolution metallicity versus the reduced equivalent width for different star samples: bulge stars (black dots), globular (orange circles) and open (red triangles) clusters from Warren & Cole (2009), and globular clusters (blue stars) from Saviane et al. (2012). Our CaT calibration is plotted as a green line, while the cubic calibration from Saviane et al. (2012) is the dashed blue line.

5. Conclusions

Using RGB and RC stars from Baade's Window, we have constructed a CaT versus $[Fe/H]$ calibration, valid in the metal-rich regime up to $[Fe/H] = +0.7$. Since bulge stars are rather sparse for $[Fe/H] < -0.5$, we used globular clusters to constrain the behaviour of the calibration relation in the metal-poor regime. We found that a single linear relation can be fitted across the whole range $-2.3 < [Fe/H] < +0.7$. A minor second-order deviation from a single linear relation, however, gives a better fit, properly taking into account the small difference between the linear best fit for globular clusters (Eq. (1)) and for bulge giants (Eq. (2)). It is worth emphasising that both globular clusters and bulge stars have $[Ca/Fe] \sim +0.3$ in the common metallicity range, therefore a possible dependence of the calibration upon the $[Ca/Fe]$ ratio would not affect the combination of the two datasets. At higher metallicities the bulge $[Ca/Fe]$ drops to zero (Gonzalez et al. 2011a, 2015), but the CaT-vs.-Fe calibration found here is still almost linear, possibly due to the combined effect of the strong saturation of CaT lines. The new calibration, represented by Eq. (3), allows one to derive the iron content of metal-rich stars by means of low-resolution spectra. The latter are the only viable way to sample a large number of stars in high-extinction regions, such as the Galactic bulge, or, in the future, in metal-rich external spheroids such as the inner halo of M 31.

Acknowledgements. We gratefully acknowledge support by the Ministry of Economy, Development, and Tourism's Millennium Science Initiative through grant IC120009, awarded to The Millennium Institute of Astrophysics (MAS), by Fondecyt Regular 1110393 and 1150345 and by the BASAL-CATA Center for Astrophysics and Associated Technologies PFB-06. S.V. acknowledges to the Henri Poincaré Junior Fellowship and the Chilean French embassy doctoral internship program to support research travels to the Nice Observatory during 2011 and 2013. G. Battaglia gratefully acknowledges financial support by the Spanish Ministry of Economy and Competitiveness (MINECO) under the Ramon y Cajal Programme (RYC-2012-11537).

References

- Alvarez, R., & Plez, B. 1998, *A&A*, **330**, 1109
- Armandroff, T. E., & Da Costa, G. S. 1991, *AJ*, **101**, 1329
- Armandroff, T. E., & Zinn, R. 1988, *AJ*, **96**, 92
- Battaglia, G., Irwin, M., Tolstoy, E., et al. 2008, *MNRAS*, **383**, 183
- Carretta, E., & Gratton, R. G. 1997, *A&AS*, **121**, 95
- Carrera, R., Gallart, C., Pancino, E., & Zinn, R. 2007, *AJ*, **134**, 1298
- Carretta, E., Bragaglia, A., Gratton, R., D'Orazi, V., & Lucatello, S. 2009, *A&A*, **508**, 695
- Carrera, R., Pancino, E., Gallart, C., & del Pino, A. 2013, *MNRAS*, **434**, 1681
- Castelli, F., & Kurucz, R. L. 2004, ArXiv e-prints [[arXiv:astro-ph/0405087](https://arxiv.org/abs/astro-ph/0405087)]
- Cenarro, A. J., Cardiel, N., Gorgas, J., et al. 2001, *MNRAS*, **326**, 959
- Cole, A. A., Smecker-Hane, T. A., Tolstoy, E., Bosler, T. L., & Gallagher, J. S. 2004, *MNRAS*, **347**, 367
- Da Costa, G. S., Held, E. V., Saviane, I., & Gullieuszik, M. 2009, *ApJ*, **705**, 1481
- Erdelyi-Mendes, M., & Barbuy, B. 1991, *A&A*, **241**, 176
- Gonzalez, O. A., Rejkuba, M., Zoccali, M., et al. 2011a, *A&A*, **530**, A54
- Gonzalez, O. A., Rejkuba, M., Zoccali, M., Valenti, E., & Minniti, D. 2011b, *A&A*, **534**, A3
- Gonzalez, O. A., Zoccali, M., Vásquez, S., et al. 2015, *A&A*, submitted
- Gustafsson, B., Edvardsson, B., Eriksson, K., et al. 2008, *A&A*, **486**, 951
- Harris, W. E. 1996, *AJ*, **112**, 1487
- Hill, V., Lecureur, A., Gomez, A., et al. 2011, *A&A*, **534**, A80
- Mashonkina, L., Korn, A. J., & Przybilla, N. 2007, *A&A*, **461**, 261
- Mauro, F., Moni Bidin, C., Geisler, D., et al. 2014, *A&A*, **563**, A76
- Minniti, D., Lucas, P. W., Emerson, J. P., et al. 2010, *New Astron.*, **15**, 433
- Mucciarelli, A., Pancino, E., Lovisi, L., Ferraro, F. R., & Lapenna, E. 2013, *ApJ*, **766**, 78
- Olszewski, E. W., Schommer, R. A., Suntzeff, N. B., & Harris, H. C. 1991, *AJ*, **101**, 515
- Rutledge, G. A., Hesser, J. E., Stetson, P. B., et al. 1997, *PASP*, **109**, 883
- Saviane, I., da Costa, G. S., Held, E. V., et al. 2012, *A&A*, **540**, A27
- Starkenburger, E., Hill, V., Tolstoy, E., et al. 2010, *A&A*, **513**, A34
- Warren, S. R., & Cole, A. A. 2009, *MNRAS*, **393**, 272
- Zinn, R., & West, M. J. 1984, *ApJS*, **55**, 45
- Zoccali, M., Hill, V., Lecureur, A., et al. 2008, *A&A*, **486**, 177
- Zoccali, M., Gonzalez, O. A., Vasquez, S., et al. 2014, *A&A*, **562**, A66
- Zoccali, M., Gonzalez, O. A., Vasquez, S., et al. 2015, *The Messenger*, **159**, 36